Supplementary Information

Control on the Long-Range Ordering of Perovskite Nanocrystal Superlattices via Thermal Regulation of Nanoconfined Water

Haney Lee,[a,‡] Seonmyeong Noh,[a,‡] Semin Kim,[a] Changsu Kim,[c] and Hyeonseok Yoon[a,b,*]

[a]Department of Polymer Engineering, Graduate School, Chonnam National University, 77 Yongbong-ro, Buk-gu, Gwangju 61186, South Korea

E-mail: hyoon@chonnam.ac.kr; Fax: +82-62-530-1779; Tel: +82-62-530-1778

[b]School of Polymer Science and Engineering, Chonnam National University, 77 Yongbong-ro, Buk-gu, Gwangju 61186, South Korea

[c]Department of Chemical and Biological Engineering, University of Wisconsin−Madison, Madison, Wisconsin 53706, United States

‡The authors equally contributed to this work

Table of Contents

(1) Chemical composition analysis of Cs-AOT prepared via ion-exchange reaction ..... -3-

(2) Morphological analysis of $CsPbBr_3$ sample in the presence of trace water..... -4-

(3) Morphological analysis of $CsPbBr_3$ sample in the absence of trace water ..... -6-

(4) Morphological analysis of CsPbBr3 samples in the absence of AOT ..... -7-

(5) Morphological analysis of CsPbBr3 samples using alternative polar solvents..... -8-

(6) Morphological analysis of $CsPbBr_3$ nanocrystals and superlattices (SLs) grown at different temperatures..... -9-

(7) Structural and spectroscopic analysis of ligand–water interactions..... -11-

(8) Investigating the presence of water molecules during the formation of $CsPbBr_3$ SLs ..... -14-

(9) Structural ordering analysis of liquid-phase-formed $CsPbBr_3$ SLs..... -15-

(10) Classical molecular dynamics simulations of ligands and metal and halide ions under trace-water conditions at different temperatures..... -17-

(11) Pattern designs..... -18-

(12) Photoluminescence (PL) comparison between nanocrystals (NCs) and SLs..... -19-

(13) Supplementary videos for **Figure 4b**..... -20-

(14) References ..... -21-

1. Chemical composition analysis of Cs-AOT prepared via ion-exchange reaction

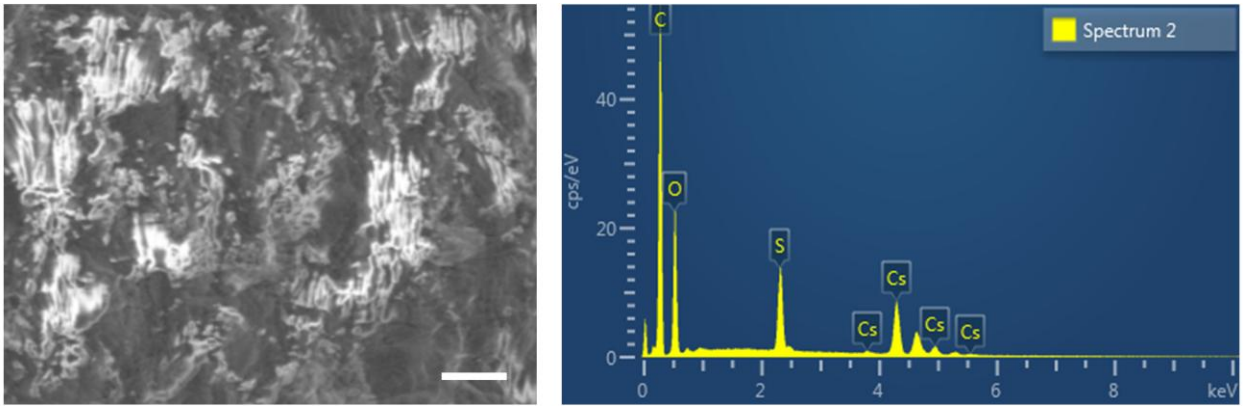

Figure S1. SEM and corresponding EDS spectrum of Cs-AOT. (left: SEM image, scale bar: 100 μm; right: EDS spectrum)

Table S1. SEM–EDS analysis of elemental atomic percentages for Cs-AOT.

Element	Atomic %
	Cs-AOT
C	72.5
O	20.2
Na	0.0
S	3.5
Cs	3.8
Total	100.0

2. Morphological analysis of $CsPbBr_3$ sample in the presence of trace water

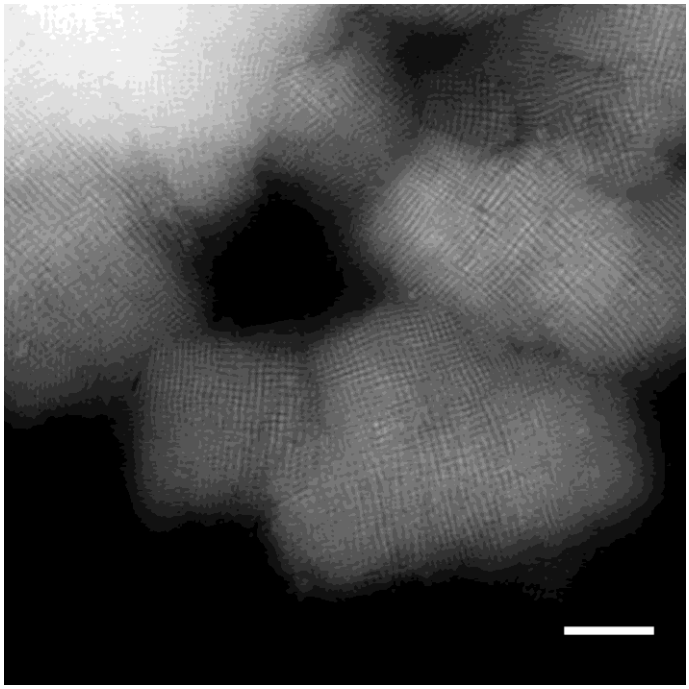

Figure S2. Dark-Field TEM image of $CsPbBr_3$ product synthesized at 110 °C in the presence of trace water (scale bar: 200 nm).

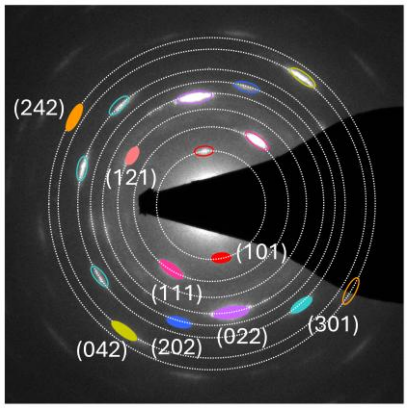

Figure S3. SAED patterns of $CsPbBr_3$ nanocrystals within SLs. The sample was prepared under the same conditions as in **Figure S2**.

3. Morphological analysis of $CsPbBr_3$ sample in the absence of trace water

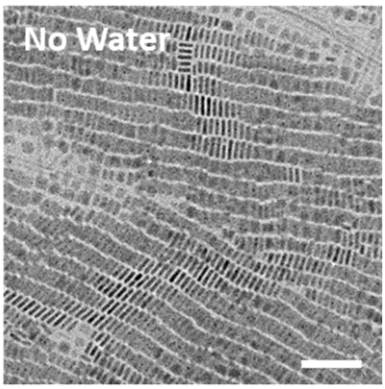

Figure S4. TEM image of $CsPbBr_3$ product synthesized at 110 °C in the absence of trace water (scale bar: 50 nm).

4. Morphological analysis of $CsPbBr_3$ samples in the absence of AOT

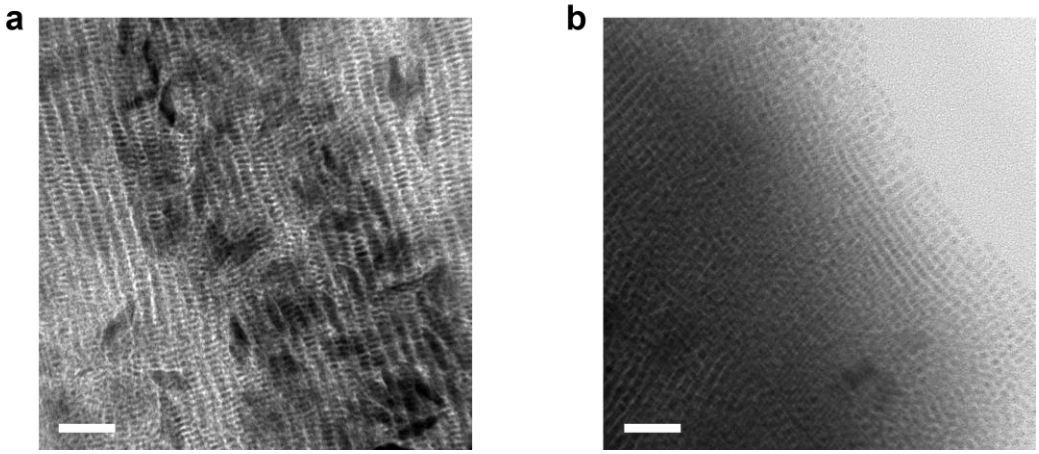

Figure S5. TEM images of $CsPbBr_3$ products synthesized at 110 °C in the absence of AOT without water (a) and with water (b; water-to-ligand ratio is 15) (scale bar: 50 nm).

5. Morphological analysis of $CsPbBr_3$ samples using alternative polar solvents

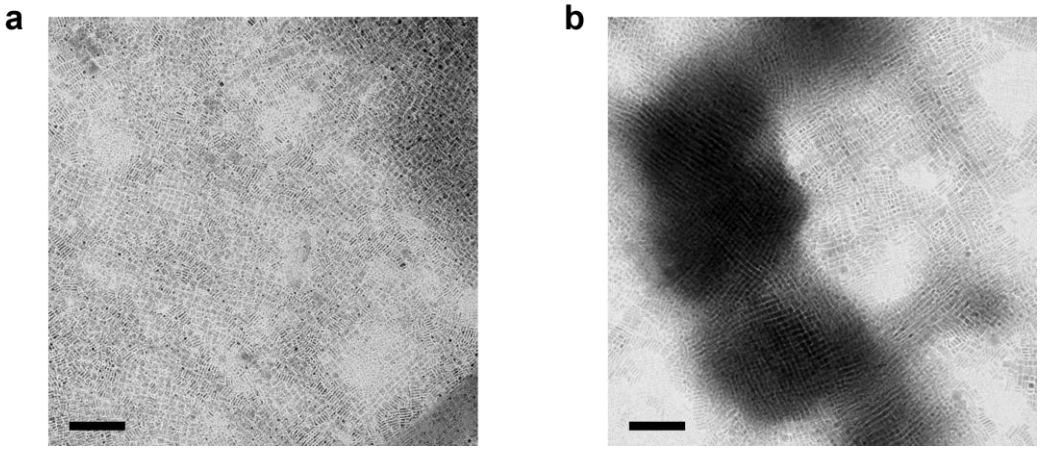

Figure S6. TEM images of $CsPbBr_3$ products synthesized at 110 °C by replacing water with polar solvents: (a) *N,N*-dimethylformamide and (b) n-propanol (scale bar: 100 nm).

6. Morphological analysis of $CsPbBr_3$ nanocrystals and superlattices (SLs) grown at different temperatures

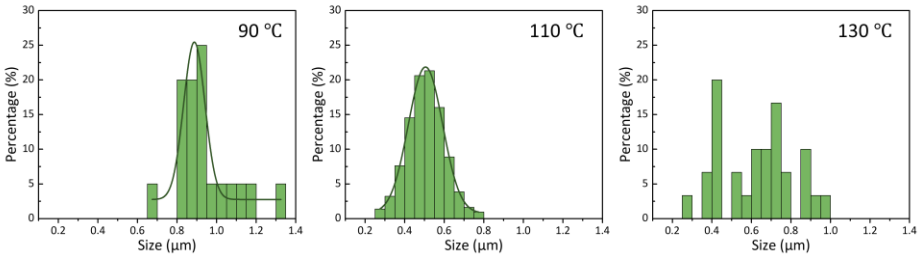

Figure S7. Size distributions of $CsPbBr_3$ SLs synthesized at different temperatures (90 to 130 °C). Sample size = 100. All the sizes were measured from TEM images in **Figure 3**.

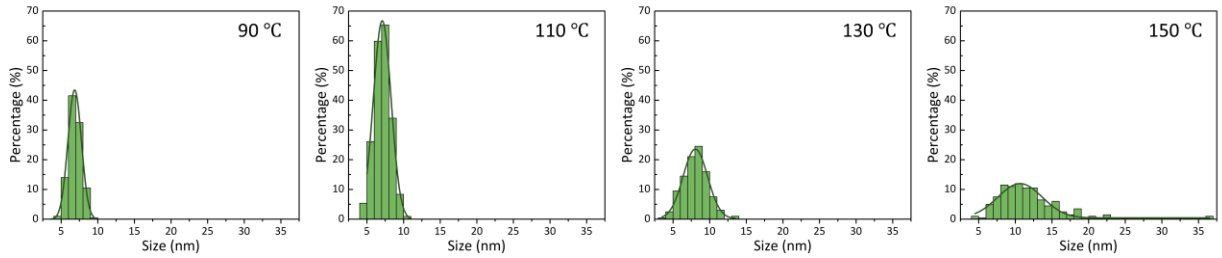

Figure S8. Size distributions of $CsPbBr_3$ nanocrystals synthesized at different temperatures (90 to 150 °C). Sample size = 200. All the sizes were measured from TEM images in **Figure 3**.

7. Structural and spectroscopic analysis of ligand–water interactions

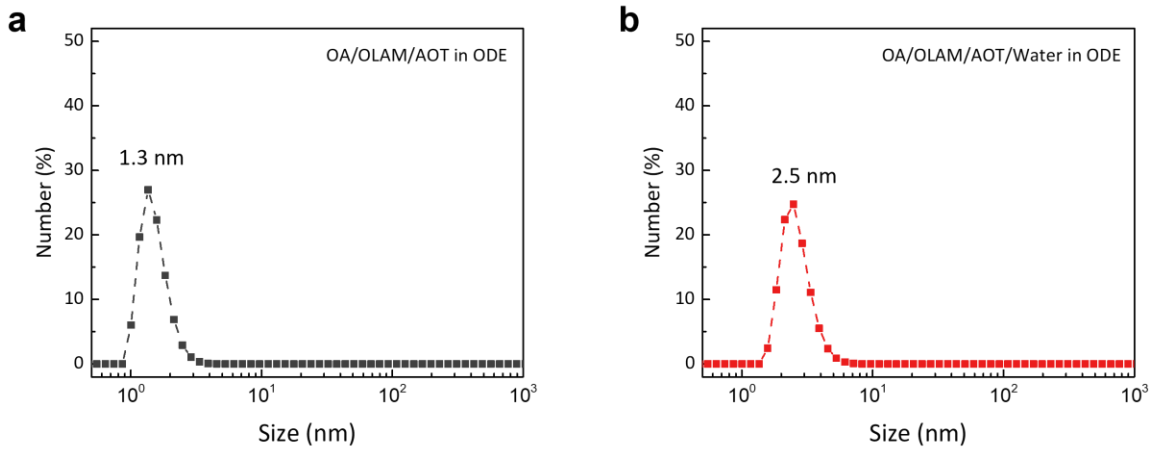

Figure S9. Dynamic light scattering (DLS) measurements to confirm the formation of reverse micelle-like environments. Size distributions of the ligand mixture (OA, OLAM, and Cs-AOT in ODE) (a) without water and (b) with water.

DLS was employed to investigate the water-ligand interactions in the nonpolar ODE environment. Without water, the DLS profile showed an average hydrodynamic diameter of ~1.3 nm. However, the presence of water led to a distinct increase in particle size (to ~2.5 nm), clearly demonstrating that water interacts with the ligands to form swollen, reverse micelle-like structures.

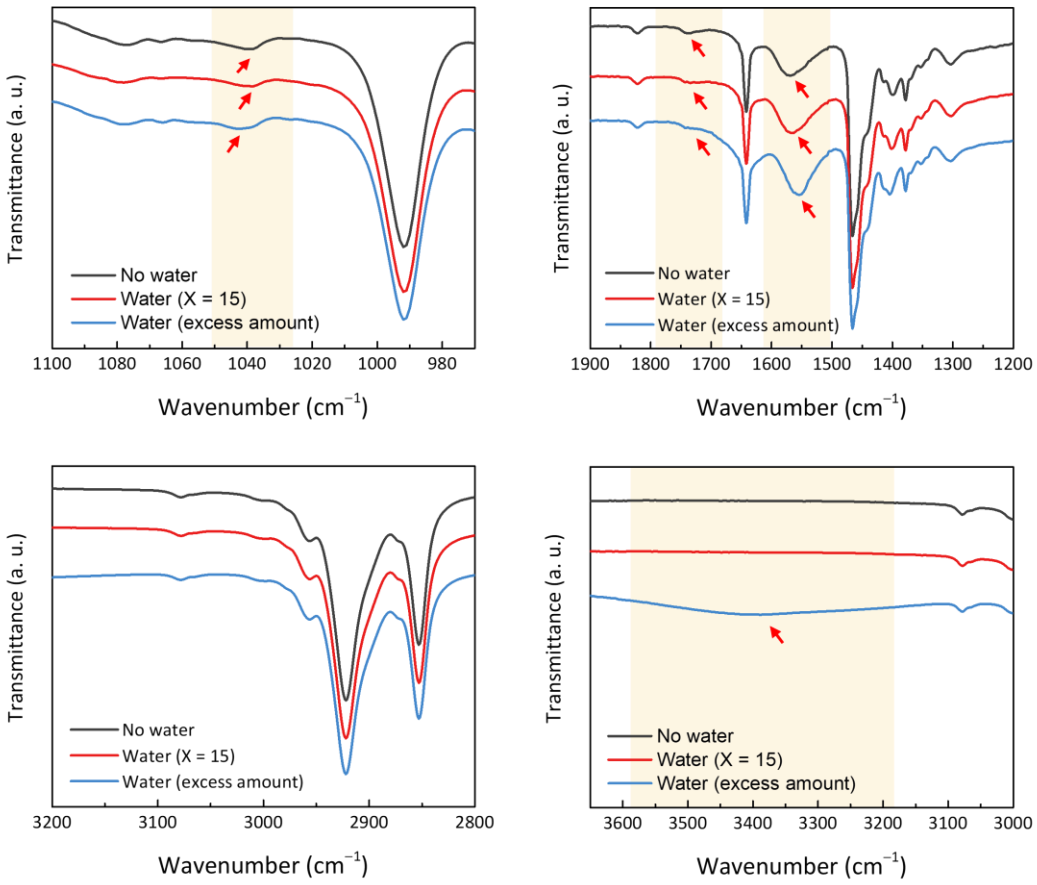

Figure S10. FT-IR spectra comparing the ligand mixtures without water, with water (X=15), and with an excess amount of water, clarifying the direct interactions between water molecules and the polar headgroups of the ligands. The spectral changes and peak shifts are highlighted and indicated by arrows.

To elucidate the specific interactions between water and the ligands, FT-IR spectroscopy was performed under varying hydration conditions. The C−H stretching vibrations in the 2800−3200 cm^{-1} region remained invariant across all samples, indicating that the structural conformation of the hydrophobic alkyl chains is not altered by the presence of water. In contrast, significant changes were observed at the polar headgroups. In the O−H stretching region (3200−3600 cm^{-1}), the characteristic broad peak of bulk water is barely visible under the optimal condition (X=15), whereas a prominent broad peak emerges when an excess amount of water is added. This

suggests that at X=15, water molecules are very rare and do not exist as free bulk water but are deeply engaged in interactions within a confined space.

These interactions are directly evidenced by the spectral changes in the functional groups. The SO_3^- symmetric stretching band of AOT at ~1040 cm^{-1} notably broadened upon water addition. Furthermore, the C=O stretching of AOT, which initially showed a major peak at ~1740 cm^{-1} without water, exhibited pronounced broadening accompanied by an increased intensity at a lower wavenumber (~1725 cm^{-1}), indicating hydrogen bonding. Similarly, the carboxylate (COO^-) peak of oleic acid displayed a clear sequential red-shift from 1571 cm^{-1} to 1568 cm^{-1}, and further to 1558 cm^{-1}. Collectively, these localized changes at the polar headgroups-coupled with the unperturbed hydrophobic tails-are highly consistent with the formation of a reverse micelle-like environment where trace water acts as a structural organizer**.**

8. Investigating the presence of water molecules during the formation of $CsPbBr_3$ SLs

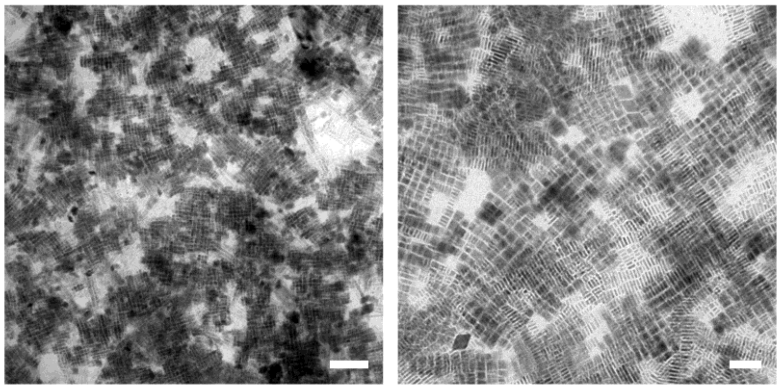

Figure S11. TEM images of $CsPbBr_3$ nanocrystals synthesized in the presence of ethanol under otherwise identical conditions to those in **Figure 1**. Scale bar: 200 nm (left) and 50 nm (right).

Water can promote the formation of reverse micelles and enhance ligand–ligand interactions, facilitating the self-assembly of SLs. However, some synthesis protocols of $CsPbBr_3$ SLs require heating above the boiling point of water, raising the possibility that water might not contribute significantly to the formation of isotropic $CsPbBr_3$ nanocrystals or their self-assembled SLs in the liquid phase. To test this possibility, ethanol, which is also a polar protic solvent with a lower boiling point, was used as an alternative. As shown in **Figure S11**, the sample prepared in the presence of ethanol produced well-dispersed $CsPbBr_3$ nanoplatelets, with a morphology nearly identical to $CsPbBr_3$ nanocrystals prepared without water. This observation suggests that ethanol evaporated under the synthesis conditions, leading to anisotropic $CsPbBr_3$ nanocrystals. These findings support that water molecules may persist during the reaction, even at synthesis temperatures above 110 °C, and may play an important role in promoting the formation of isotropic $CsPbBr_3$ nanocubes and their ordered SLs.

9. Structural ordering analysis of liquid-phase-formed $CsPbBr_3$ SLs

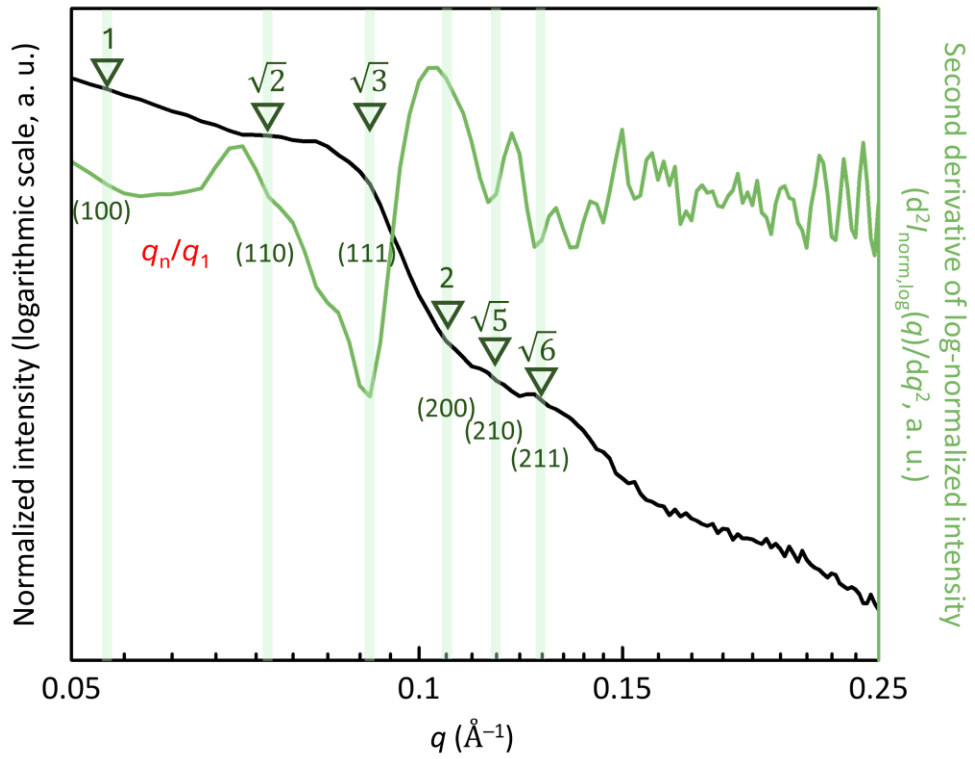

Figure S12. SAXS plot of $CsPbBr_3$ SLs synthesized at 90 °C in the presence of trace water, including both the scattering curve and the corresponding numerical second-derivative curve. The second-derivative curve was obtained from the SAXS data after applying a three-point moving average (repeated three times) for noise reduction. Vertical lines are included only as guides to the eye.

SLs dispersed in the liquid phase may show weak diffraction features in SAXS measurements.[1] To resolve the subtle signals, the SAXS data were smoothed using a three-point moving average applied three consecutive times to suppress noise. The numerical second derivative of the SAXS intensity was then calculated using the following central difference formula:

$$I''(q_i) \approx \frac{I(q_{i+1}) - 2I(q_i) + I(q_{i-1})}{(\Delta q)^2}$$

This analysis enhances the visibility of weak diffraction peaks that are difficult to identify directly from the raw SAXS profiles.

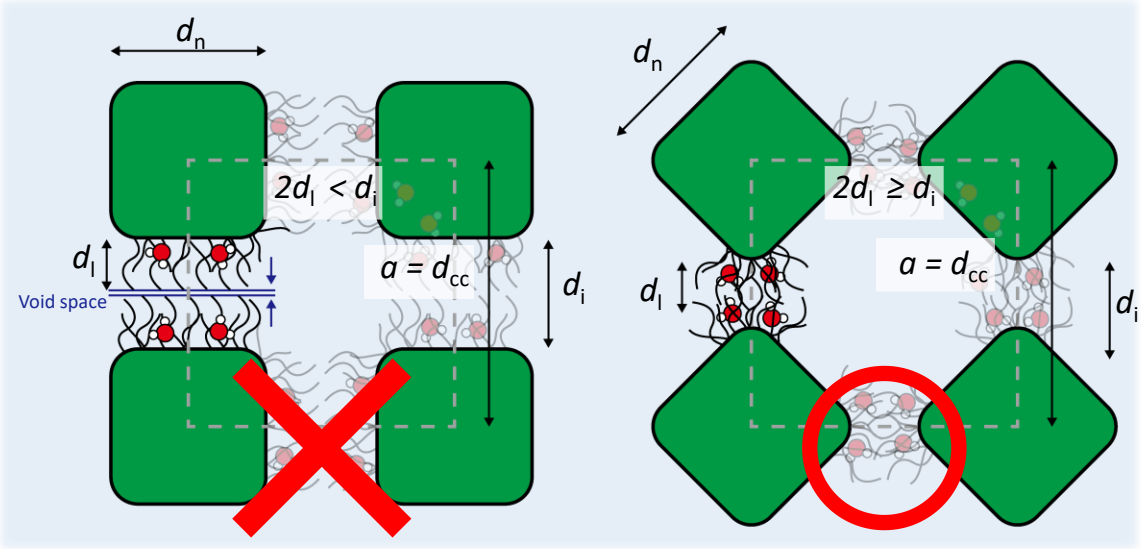

Figure S13. Illustration of the unit cell analysis for the simple cubic (SC) $CsPbBr_3$ SLs. (Left) non-tilted nanocrystals in SC unit cell; (Right) tilted nanocrystals in SC unit cell. Green cubes, black curves, light gray dashed box represent $CsPbBr_3$ nanocrystals, ligands, and the unit cell, respectively. Red and white circles denote oxygen and hydrogen atoms, respectively. d_n, d_l, d_i, d_{cc}, and a correspond to the nanocrystal diameter, maximum ligand length, interparticle spacing, interparticle center-to-center distance, lattice parameter, respectively.

At 90 °C, the SAXS pattern showed the structural ordering of SC $CsPbBr_3$ SLs (**Figure S12**). The scattering vectors were assigned as q_1, q_2, q_3,q_4, q_5, and q_6 at 0.052, 0.073, 0.090, 0.104, 0.116, and 0.127 $Å^{-1}$, respectively, corresponding to q_n/q_1 ratios of 1, $\sqrt{2}$, $\sqrt{3}$, 2,$\sqrt{5}$, and $\sqrt{6}$. Notably, the (111) and (210) peaks were pronounced, which is likely due to tilted nanocrystals within the SC unit cell.[2] To evaluate whether this structural model is appropriate, we estimated the unit cell parameters for both non-tilted and tilted nanocrystals in the SC unit cells. d_n was 6.9 nm (**Figure S8**). d_{cc} (from $d_{cc} = 2\pi/10q_1 \approx a$ in SC) was 12.1 nm, and d_l was 2.3 nm. For the non-tilted case, d_i was 5.2 nm, which is larger than $2d_l$ (4.6 nm). This suggests that ligand–ligand interaction between nanocrystals would be limited, making the formation of SC SLs less likely, as illustrated in **Figure S13**. In contrast, for the tilted case, d_i was 2.3 nm, which is smaller than $2d_l$. This suggests significant ligand interaction in the tilted case, consistent with a model in which SC SLs form from tilted nanocrystals in solution.

10. Classical molecular dynamics simulations of ligands and metal and halide ions under trace-water conditions at different temperatures

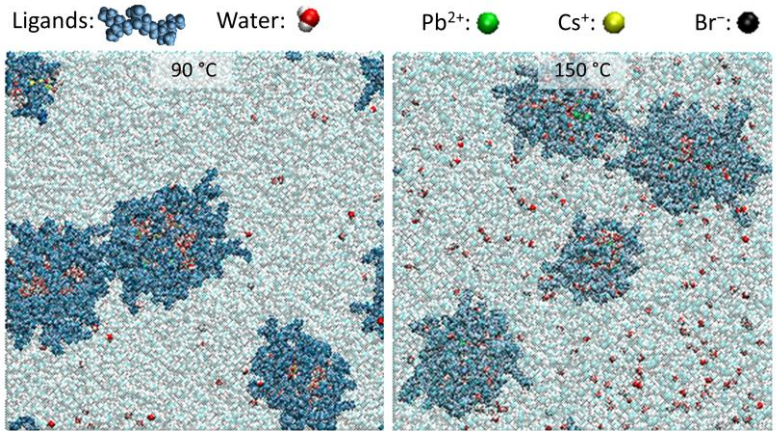

Figure S14. Snapshots from MD simulations illustrating the distribution of metal and halide ions (Cs^+, Pb^{2+}, and Br^-), and ligands (OA and OLAM) in ODE at 40 ns at (left) 90 and (right) 150 °C. Visualization showing ODE solvent, ligands, and undistinguished ions in the legend.

11. Pattern designs

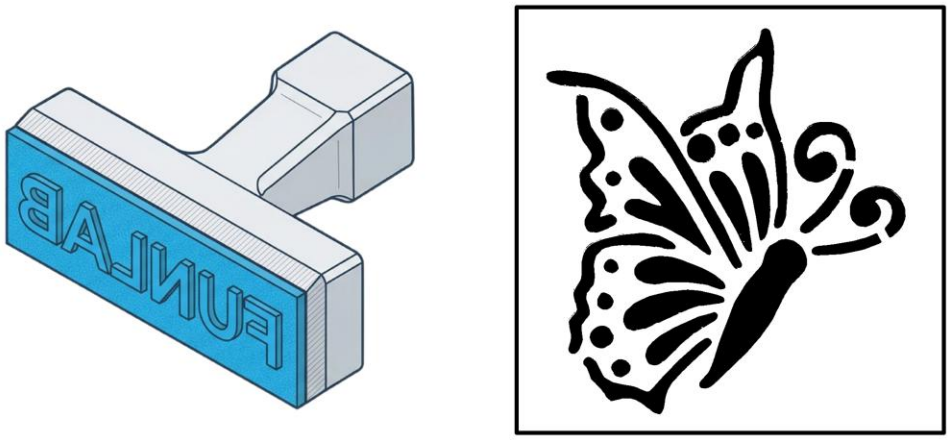

Figure S15. Schematic illustration of the printed patterns for stamp transfer and film fabrication.

12. Photoluminescence (PL) comparison between nanocrystals (NCs) and SLs

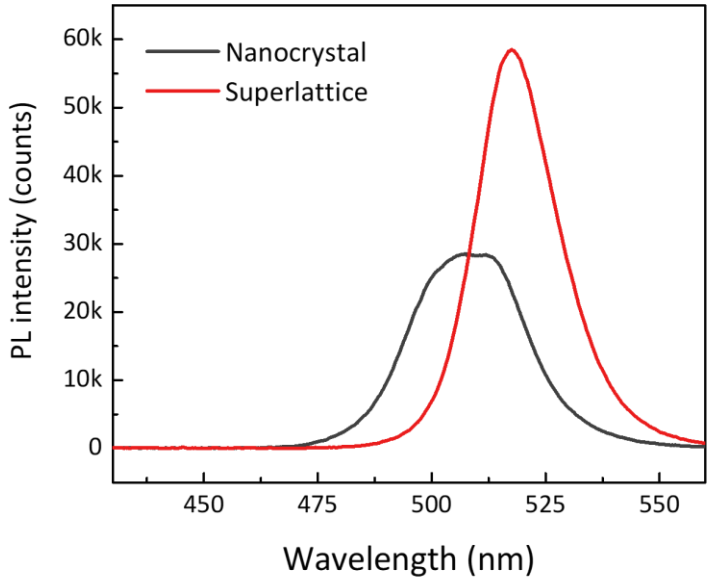

Figure S16. PL spectra of NCs and SLs.

To evaluate the optical properties, NCs and SLs at identical concentrations were respectively dispersed in a poly(ethylene-co-vinyl acetate) (EVA)/toluene solution via vortex mixing. The mixtures were thoroughly degassed over a sufficient period without any additional physical agitation to preserve their structures. Upon excitation at 400 nm, the PL spectra exhibited distinct emission profiles. The individual NCs displayed a broad emission peak at 507 nm, whereas the SLs exhibited a relatively sharp peak at 517 nm. Furthermore, a notable difference in PL intensity was observed; the emission intensities of the NCs and SLs were approximately 28.4k and 58.5k (counts), respectively, demonstrating a significant enhancement in the SLs.

13. Supplementary videos for Figure 4b

Supplementary Video 1. MD trajectory at 90 °C corresponding to **Figure 4b**, showing the time evolution of the distributions of metal ions (Cs and Pb), halide ions (Br), AOT, co-ligands (OA and OLAM), and water. ODE is omitted for clarity.

Supplementary Video 2. MD trajectory at 150 °C corresponding to **Figure 4b**, showing the time evolution of the distributions of metal ions (Cs and Pb), halide ions (Br), AOT, co-ligands (OA and OLAM), and water. ODE is omitted for clarity.

14. References

1. J. Tian, T.-Y. Zhou, S.-C. Zhang, S. Aloni, M. V. Altoe, S.-H. Xie, H. Wang, D.-W. Zhang, X. Zhao, Y. Liu and Z.-T. Li, Three-dimensional periodic supramolecular organic framework ion sponge in water and microcrystals, *Nat. Commun.*, 2014, **5**, 5574.
2. Z.-P. Lv, M. Kapuscinski, G. Járvás, S. Yu and L. Bergström, Time-Resolved SAXS Study of Polarity- and Surfactant-Controlled Superlattice Transformations of Oleate-Capped Nanocubes During Solvent Removal, *Small*, 2022, **18**, 2106768.